Available online at www.sciencedirect.com
SCIENCE DIRECT®
Journal of Computational Physics 202 (2005) 507–532
JOURNAL OF COMPUTATIONAL PHYSICS
www.elsevier.com/locate/jcp

On the sonic point glitch

Huazhong Tang

LMAM, School of Mathematical Sciences, Peking University, Beijing 100871, PR China

Received 2 April 2004; received in revised form 14 July 2004; accepted 15 July 2004
Available online 21 September 2004

Abstract

This paper presents theoretical and numerical analyses of the sonic point glitch based on some numerical schemes for the Burgers' equation and the Euler equations in fluid mechanics. The sonic glitch is formed in the sonic rarefaction fan. It has no any direct connection with the violation of the entropy condition or the size of numerical viscosity of a finite-difference scheme. Our results show that it is mainly coming from a disparity in wave speeds across the sonic point. If numerical viscosity depends on the characteristic direction, then the disparity may be formed between the numerical and physical wave speeds around the sonic point, and triggers the sonic wiggle in the numerical solution. We also find that the initial data reconstruction technique of van Leer can effectively eliminate the flaw around the sonic point for the Burgers' equation. Some other possible cures are also suggested.

Keywords: Upwind scheme; Compressible flow; Sonic point glitch; Riemann solver

1. Introduction

Although much attention has been paid to capture shock waves and contact discontinuities, the proper resolution of rarefaction wave has also proved to be difficult. For example, even in the smooth flow region, such as a high speed expansion wave passing through a corner, the sonic glitch or the so-called "dog-leg" phenomenon, see Fig. 1, has occasionally been observed by Woodward and Colella [29], when they solved an inviscid flow in a channel containing a forward step. There are other cases, e.g. diffraction of shock waves in [11,13] and supersonic flows past a circular cylinder [15] where the sonic glitch can arise. Glitches do not really occur along sonic lines in multi-dimensional flows but only where the normal speed component is sonic.

E-mail address: hztang@math.pku.edu.cn.

0021-9991/$ - see front matter
doi:10.1016/j.jcp.2004.07.013

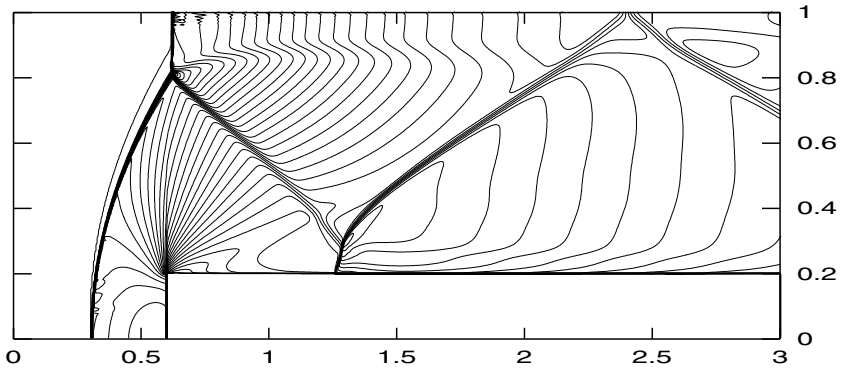

Fig. 1. Density contours with 32 equally spaced contour lines for the Mach 3 wind tunnel problem [29] calculated by using first-order accurate Godunov scheme on a uniform grid with $\Delta x = \Delta y = 1/200$. The so-called "dog-leg" phenomenon has been observed near the sonic line above the corner of the forward step, i.e. the point (0.6,0.2).

The sonic glitch arises only in the presence of sonic rarefaction waves and is a small non-physically discontinuous jump or any visible error around the sonic point generated by numerical methods within a sonic rarefaction wave. If the discrete scheme admits expansion shocks, an arbitrarily large jump may be found where one expects a smooth transition through the sonic point [27]. Toro [24] observed that the sonic glitch was associated with almost all upwind shock capturing schemes applied to nonlinear hyperbolic conservation laws. These schemes are the Godunov method [4], the Engquist–Osher scheme [3,14], the Roe method [17], and the flux vector splitting (FVS) schemes of Steger and Warming [20], van Leer [26], and Liou and Steffen [8], etc. Another name for the sonic glitch in the literature is the so-called "entropy glitch", which seems implicitly to point out the relation between the sonic glitch and the entropy condition [2,24].

Several authors have paid their attention to sonic-point capturing. van Leer et al. [28] devised a sonic-point capturing scheme for a hyperbolic system of equations incorporating a source terms by balancing the flux derivative and the source term in both forward- and backward-moving parts of the transonic expansion fan. An effective absolute value introduced by them is precisely equivalent to the modified absolute value proposed by Harten [5], see (2.25). Roe [18] gave a close study of the scalar case and a corresponding extension to the case of a system of equations. According to the decay rate criterion, he modified the numerical fluxes of first-order and second-order upwind schemes in different ways. In order to obtain good results, the numerical flux of first-order schemes is modified at the sonic point and at both of its neighbors, but modification of second-order schemes is done only at the sonic point. Liu and Liou [9] proposed a new calculation method for the eigenvalues at the cell interface and gave smooth transonic solutions to several one- and two-dimensional problems. The new positive and negative eigenvalues at the sonic cell face are continuous, and equal to the old ones in the non-sonic region such that the scheme accuracy remains essentially unchanged. Recently, Moschetta and Gressier [10,11] showed that the sonic glitch was not due to the non-smoothness of the flux function in the approximate Riemann solutions at the sonic point. Based on the different numerical performance of the gas-kinetic schemes and the upwind-differencing schemes around the sonic point, they tried to fix the glitch by borrowing a kinetic pressure correction term from the gas-kinetic scheme and applied it to the upwind-differencing schemes. Up to now, to our knowledge, no explicit reason for the glitch formation was given there.

In this paper, according to theoretical and numerical analyses of the sonic point glitch based on several numerical schemes for the inviscid Burgers' equation and the Euler equations, for the first time we are going to point out the physical reason underlying the sonic glitch. Our results will show that if numerical viscosity

of a numerical scheme depends on the characteristic direction, then the disparity may be produced between the numerical and physical wave speeds around the sonic point, and the sonic wiggle is triggered in the sonic rarefaction fan due to slower approximate wave speeds. Moreover, we also show that van Leer's MUSCL (monotonic upstream-centered scheme for conservation laws) scheme [25] for the Burgers' equation does not produce the sonic glitch, but Harten's TVD (total variation diminishing) scheme [5] cannot do it. Some other possible cures are also considered.

This paper is organized as follows. In Section 2, we study the formation of the sonic glitch in the case of the inviscid Burgers' equation. Several well-known schemes are analyzed theoretically and numerically for almost all possible cases. Section 3 analyzes the formation of the sonic glitch in the Euler equations of gas dynamics. It is a mimic extension of the result in form given in Section 2. Several possible cures of the sonic glitch are also suggested there. We conclude the paper with a few remarks in Section 4.

2. The sonic glitch in the Burgers' Equation

Consider one-dimensional Burgers' equation in the inviscid limit

$$\frac{\partial u}{\partial t}+\frac{\partial f(u)}{\partial x}=0, \tag{2.1}$$

with $f(u)=\frac{1}{2}u^2$ and initial data $u(x,0)=u_0(x)$, where $u_0(x)$ is a given function, $x\in\mathbb{R}$ and $t>0$.

For hyperbolic conservation laws, the simplest and useful initial value problem is the so-called Riemann problem for which initial data are of the following form:

$$u_0(x)=\begin{cases} u_{\mathrm{L}}, & x<0,\\ u_{\mathrm{R}}, & x>0, \end{cases} \tag{2.2}$$

where u_{L} and u_{R} are two constants. Its solution will be a fundamental component of Godunov type scheme. The solution $u(x,t)$ to the Riemann problem (2.1) and (2.2) can be given in an explicit form. It is: (i) a rarefaction wave solution

$$u(x,t)=\begin{cases} u_{\mathrm{L}}, & x<u_{\mathrm{L}}t,\\ \frac{x}{t}, & u_{\mathrm{L}}t\leqslant x\leqslant u_{\mathrm{R}}t,\\ u_{\mathrm{R}}, & x>u_{\mathrm{R}}t, \end{cases} \tag{2.3}$$

if $u_{\mathrm{L}}<u_{\mathrm{R}}$; (ii) a shock wave solution

$$u(x,t)=\begin{cases} u_{\mathrm{L}}, & x<st,\\ u_{\mathrm{R}}, & x>st, \end{cases} \tag{2.4}$$

if $u_{\mathrm{L}}>u_{\mathrm{R}}$, where s denotes speed of shock wave satisfying

$$s(u_{\mathrm{L}}-u_{\mathrm{R}})=f(u_{\mathrm{L}})-f(u_{\mathrm{R}}).$$

The sonic point corresponds to a point with $f'(u)\equiv u=0$, and the location of this point is fixed in space due to its diminishing wave speed. Thus, for the Riemann problem (2.1) and (2.2), if $u_L<0<u_{\mathrm{R}}$ or $u_{\mathrm{L}}>0>u_{\mathrm{R}}$, the solution given in (2.3) or (2.4) is corresponding to a transonic solution. Generally, the sonic glitch does not arise in any transonic compression region. To confirm it, we do a numerical experiment on computation of a 2π-periodic problem of the Burgers' equation, see [21], where the 2π-periodic initial data are given as follows:

$$u_0(x)\equiv 0.5+\sin(x),\quad x\in[0,2\pi).$$

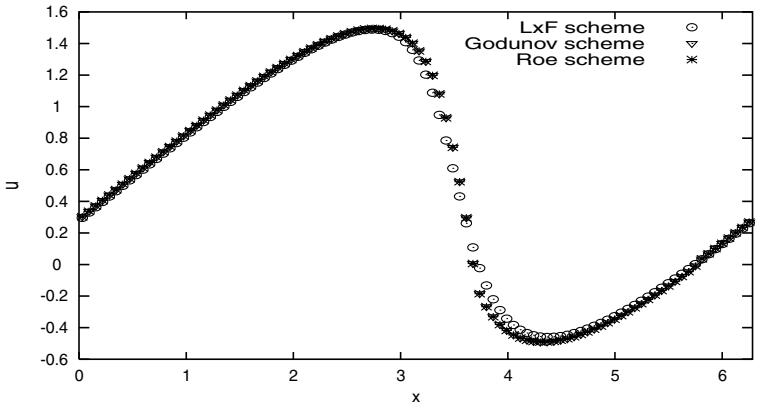

Fig. 2. The computed solutions of the Burgers' equation at $t = 0.8$ containing a transonic compression wave. They are calculated by using the LxF scheme, the Godunov scheme (2.14), and the Roe scheme, respectively.

Fig. 2 shows the numerical solutions with a resolution of 100 grid cells, calculated by using three first-order accurate schemes, the Godunov method, the Roe scheme, and the Lax–Friedrichs (LxF) scheme, respectively.

There is a transonic compression wave in the solution at $t = 0.8$ in the interval $[2.8, 4.2]$ before the shock is formed. Obviously, the sonic glitch is not shown in the computed solution. The reason for that will be analyzed later in this section.

2.1. The Godunov scheme

In the following, we begin to investigate numerical evolution of the sonic rarefaction wave (2.3) with $u_L < 0 < u_R$. Unless stated otherwise, we will take $u_R = -u_L = 1$. Give a uniform partition of the physical domain $\mathbb{R}$, $x_j = jh$, where h denotes a cell size in space, and $j \in \mathbb{Z}$. The initial value function $u(x,0) = u_0(x)$ will be approximated by the cell average over each cell $I_j = \{x | x_j - \frac{h}{2} < x < x_j + \frac{h}{2}\}$, i.e.

$$u_h(x,0) = \frac{1}{h}\int_{I_j} u_0(x)\,dx =: u_j^0 \quad \text{for } x \in I_j. \tag{2.5}$$

We assume that the solution at time t_n to the Riemann problem of the Burgers' equation (2.1) and (2.2) is given exactly, i.e.

$$u(x,t_n) = \begin{cases} u_L, & x < u_L t_n, \\ \frac{x}{t_n}, & u_L t_n \leqslant x \leqslant u_R t_n, \\ u_R, & x > u_R t_n, \end{cases} \tag{2.6}$$

and the time step size τ satisfies the CFL condition:

$$\sigma \max_u \{|a(u)|\} \leqslant \mu < 1, \tag{2.7}$$

where $\sigma = \tau/h$, μ is the Courant number, and $a(u)$ denotes the characteristic speed, $a(u) = f'(u)$.

In order to evolve numerically this sonic rarefaction wave, we should project the initial data (2.6) onto the given uniform grid, following (2.5). Thus, we can represent numerically the initial data (2.6) as a constant state inside each cell I_j. For example, within the expansion fan but away from its two corners, the tail and the head, the initial data inside the cell I_j are approximated by

$$u_j^n = \frac{1}{h}\int_{I_j} \frac{x}{t_n}\,\mathrm{d}x \equiv \frac{x_j}{t_n}. \tag{2.8}$$

These constant states at the right-hand side of the sonic point satisfy $u_j > 0$ and $u_j < 0$ at the left. At a later time $t_{n+1} = t_n + \tau$, the exact solution becomes

$$u(x,t_{n+1}) = \begin{cases} u_{\mathrm{L}}, & x < u_{\mathrm{L}} t_{n+1}, \\ \frac{x}{t_n+\tau}, & u_{\mathrm{L}} t_{n+1} \leqslant x \leqslant u_{\mathrm{R}} t_{n+1}, \\ u_{\mathrm{R}}, & x > u_{\mathrm{R}} t_{n+1}, \end{cases} \tag{2.9}$$

and the corresponding exact cell-averaged value is

$$u_j^{\mathrm{e}} = \frac{x_j}{t_n+\tau} = \frac{x_j}{t_n}\left(\frac{1}{1+\tau/t_n}\right) = \frac{x_j}{t_n}\left(1 - \frac{\tau}{t_n} + \left(\frac{\tau}{t_n}\right)^2 - \left(\frac{\tau}{t_n}\right)^3 + \cdots\right), \tag{2.10}$$

where the superscript e means the exact solution.

The Godunov method for (2.1) can be written in a conservation form:

$$u_j^{n+1} = u_j^n - \sigma\left(\hat{f}^G(u_j^n, u_{j+1}^n) - \hat{f}^G(u_{j-1}^n, u_j^n)\right), \tag{2.11}$$

where

$$\hat{f}^G(u_j^n, u_{j+1}^n) = f\left(v(0; u_j, u_{j+1})\right), \tag{2.12}$$

and $v(x/t;u_j,u_{j+1})$ denotes the (weak) similarity solution to the Riemann problem of (2.1) with initial data

$$u(x,t_n) = \begin{cases} u_j, & x < x_{j+\frac{1}{2}}, \\ u_{j+1}, & x > x_{j+\frac{1}{2}}. \end{cases} \tag{2.13}$$

It means that the Godunov method (2.11) and (2.12) updates the flow variable inside each cell by solving the exact Riemann problem of (2.1) at each cell boundary $x_{j+\frac{1}{2}}$. For the in-viscid Burgers' equation, we may have, see [27],

$$\hat{f}^G(u_j^n, u_{j+1}^n) = \max\left\{\frac{1}{2}(u_j^+)^2, \frac{1}{2}(u_{j+1}^-)^2\right\}, \tag{2.14}$$

where $u^+ = \max\{u,0\}$ and $u^- = \min\{u,0\}$.

Therefore, on the right-hand side of the sonic point, $t_n - h > x_j > h$, the flow variable is updated by using the Godunov scheme through

$$u_j^{n+1} = u_j^n + \sigma\left(\widehat{f}_{j-\frac{1}{2}} - \widehat{f}_{j+\frac{1}{2}}\right) = \frac{x_j}{t_n} + \sigma\left(\frac{1}{2}\left(\frac{x_{j-1}}{t_n}\right)^2 - \frac{1}{2}\left(\frac{x_j}{t_n}\right)^2\right) = \frac{x_j}{t_n}\left(1 - \frac{\tau}{t_n}\right) + \frac{\tau h}{2(t_n)^2}, \tag{2.15}$$

and on the left side, $-t_n + h < x_j < -h$, it is

$$u_j^{n+1} = u_j^n + \sigma\left(\widehat{f}_{j-\frac{1}{2}} - \widehat{f}_{j+\frac{1}{2}}\right) = \frac{x_j}{t_n} + \sigma\left(\frac{1}{2}\left(\frac{x_j}{t_n}\right)^2 - \frac{1}{2}\left(\frac{x_{j+1}}{t_n}\right)^2\right) = \frac{x_j}{t_n}\left(1 - \frac{\tau}{t_n}\right) - \frac{\tau h}{2(t_n)^2}. \tag{2.16}$$

If we define

$$\widetilde{u}_j^{\mathrm{e}} = \frac{x_j}{t_n}\left(1 - \frac{\tau}{t_n}\right) = u_j^{\mathrm{e}} + \mathcal{O}(\tau^2),$$

then we can find from (2.15) and (2.16) that after one time step, the numerical solution u_j^{n+1} is bigger than the "exact" one $\widetilde{u}_j^{\mathrm{e}}$ in the region $t_n - h > x_j > h$, while smaller than $\widetilde{u}_j^{\mathrm{e}}$ in the region $-t_n + h < x_j < -h$. Unfortunately, the shift appeared in the approximate solution has opposite signs in the two regions: $x > h$ and $x < -h$. Therefore, a jump with the magnitude of $\tau h/(t_n)^2$ will appear at the sonic point $x = 0$ after one evolution time step. As a result, the approximate solution will move upward (or downward) in comparison with the "exact" one in the right (or left) region at the next time step. Moreover, the strength of this jump will tend to zero, as the space size h tends to zero.

Remark 2.1. In the above, $\widetilde{u}_j^{\mathrm{e}}$ is a second-order accurate approximation of the exact solution u_j^{e} in time. It is possible to improve it by using a higher-order Runge–Kutta time discretization. But, the magnitude of the relative error $u_j^{n+1} - \widetilde{u}_j^{\mathrm{e}}$ is $\mathcal{O}(h)$.

An alternative way to understand the sonic glitch formation can be the following. Because the solution is smooth within the expansion fan, Eq. (2.1) can be rewritten in a non-conservative form as follows:

$$\frac{\partial u}{\partial t} + a(u)\frac{\partial u}{\partial x} = 0, \quad a(u) = f'(u) \equiv u. \tag{2.17}$$

Hence, the exact wave speed at x_j equals to $u_j^n = x_j/t_n$ when t belongs to the time interval $[t_n, t_n + \tau)$. On the other hand, (2.15) and (2.16) can also be rewritten in a non-conservative form as a finite-difference approximation of (2.17)

$$u_j^{n+1} = \begin{cases} \frac{x_j}{t_n} + \sigma\frac{x_j + x_{j-1}}{2t_n}\left(\frac{x_{j-1}}{t_n} - \frac{x_j}{t_n}\right) & \text{for (2.15)}, \\ \frac{x_j}{t_n} + \sigma\frac{x_j + x_{j+1}}{2t_n}\left(\frac{x_j}{t_n} - \frac{x_{j+1}}{t_n}\right) & \text{for (2.16)}. \end{cases} \tag{2.18}$$

Due to the upwind flux (2.14) at a cell interface, the numerical wave propagation speed at x_j becomes $(x_j + x_{j-1})/2t_n$ for $x_j > h$, and $(x_j + x_{j+1})/2t_n$ for $x_j < -h$. Comparing them with the exact wave speed, we can find that the magnitude of the numerical wave speed is smaller than the exact wave speed in both regions, that is to say, $0 < (x_j + x_{j-1})/2t_n < x_j/t_n$ in the region $x > h$ and $x_j/t_n < (x_j + x_{j+1})/2t_n < 0$ in the region $x < h$. It is worth noting that the speed difference, $h/2t_n$, is independent of the distance to the sonic point. So, the propagation of the approximate solution undergoes a delay around the sonic point and generates a wiggle there due to slower wave speeds. Using exact value of the wave speeds to replace the numerical ones in (2.18), we may expect to avoid appearance of the sonic glitch. In fact, we have:

$$u_j^{n+1} = \begin{cases} \frac{x_j}{t_n} + \sigma\frac{x_j}{t_n}\left(\frac{x_{j-1}}{t_n} - \frac{x_j}{t_n}\right) = \frac{x_j}{t_n}\left(1 - \frac{\Delta t}{t_n}\right) & \text{for } u_j^n \geqslant 0, \\ \frac{x_j}{t_n} + \sigma\frac{x_j}{t_n}\left(\frac{x_j}{t_n} - \frac{x_{j+1}}{t_n}\right) = \frac{x_j}{t_n}\left(1 - \frac{\Delta t}{t_n}\right) & \text{for } u_j^n < 0. \end{cases} \tag{2.19}$$

To validate the theoretical analysis, some numerical experiments are conducted here. We take $t_n = 0.1$, $\mu = 0.9$, and 150 cells. Figs. 3 and 4 show the numerical solutions ("circle") at $t = t_n + 0.9$ calculated by using the Godunov method and the Roe scheme, respectively. For comparison, the exact solution ("solid line") is also given there. Obviously, the sonic glitch is formed around the sonic point $x = 0$. It is in accordance with the theoretical one. The jump around the sonic point in Fig. 4 becomes very large such that the numerical solution is unacceptable. In Fig. 5 we give the corresponding actual error plots. The result shows that because local maximum or minimum errors are formed around the sonic point, the error distributions and the numerical solutions are not monotone with respect to x/t within the expansion fan, i.e. the interval $(-1,1)$. These errors should tend to zero, as $h \to 0$. In Fig. 6, we plot the local maximum error around the sonic point versus the space size in a log scale. Its slope equals approximately to 0.987 that is a numerical measure of the scheme accuracy. For a rarefaction wave without a sonic point in it, such as a wave with u

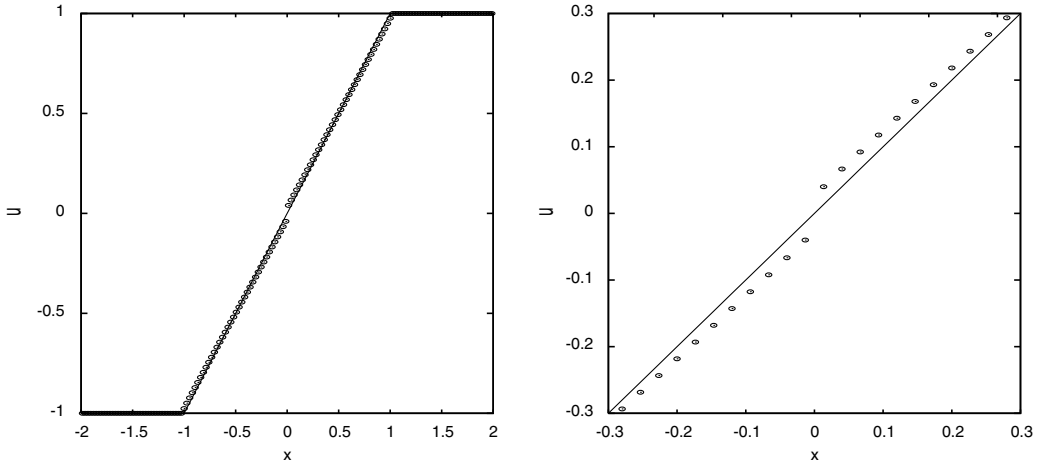

Fig. 3. The computed solutions (“circle”) of the Burgers’ equation at $t = t_n + 0.9$ are given by using the Godunov scheme (2.11) and (2.12) with 150 grid cells and $t_n = 0.1$. The solid line denotes the exact solution. Left: the solution within the global domain $[-2, 2]$; right: close-up of the solution in the vicinity of the sonic point.

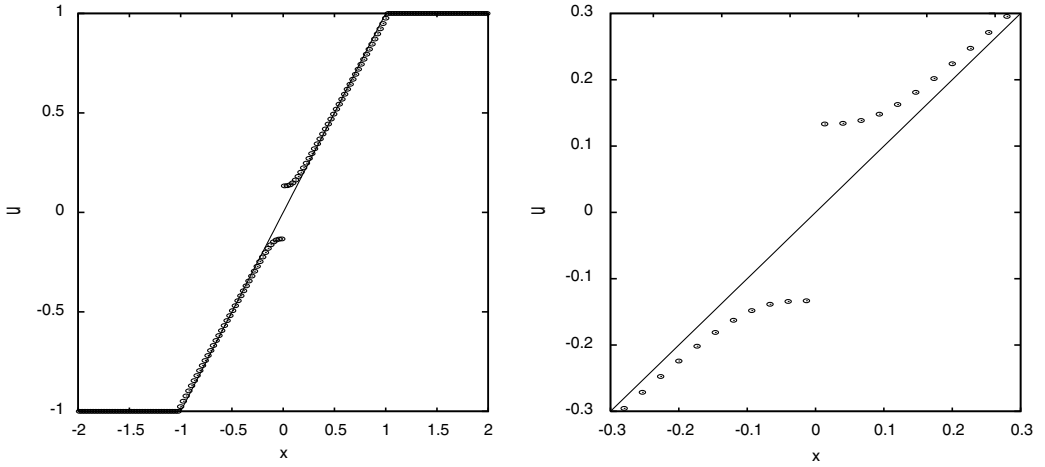

Fig. 4. Same as Fig. 3, except for the Roe scheme.

going from $u_L = 0.1$ to $u_R = 1.1$, the uniform upward shift $u_j^{n+1} - u_j^e$ in this case will not generate any glitch in this rarefaction wave, see Fig. 7.

Remark 2.2. The above analysis could be applied to the transonic compression problem of the Burgers’ equation. For convenience, we take initial data (at $t = t_n$) as

$$u(x, t_n) = \begin{cases} u_L, & x < x_L, \\ -\frac{x}{t_n}, & x_L \leqslant x \leqslant x_R, \\ u_R, & x > x_R, \end{cases} \tag{2.20}$$

where $u_L = -x_L/t_n > 0 > -x_R/t_n = u_R$, $t_n > 0$. Assuming that $-x_L$ and x_R are big enough such that the solution to the Cauchy problem (2.1) and (2.20) is smooth within the sub-domain $[t_n, t_n + \tau] \times (x_L, x_R)$, we may

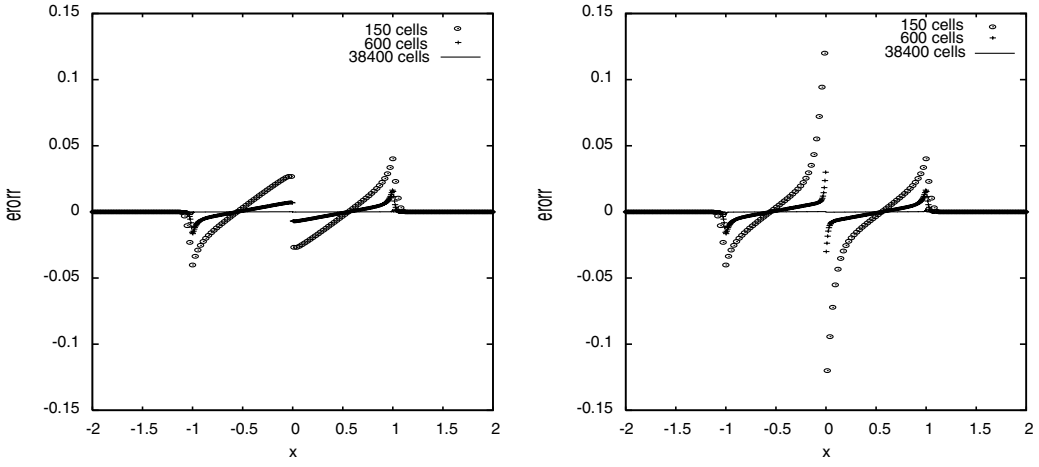

Fig. 5. The error distributions, $u(x_j, t_n) - u_j^n$, for the Burger's equation. Left: the Godunov scheme; right: the Roe scheme.

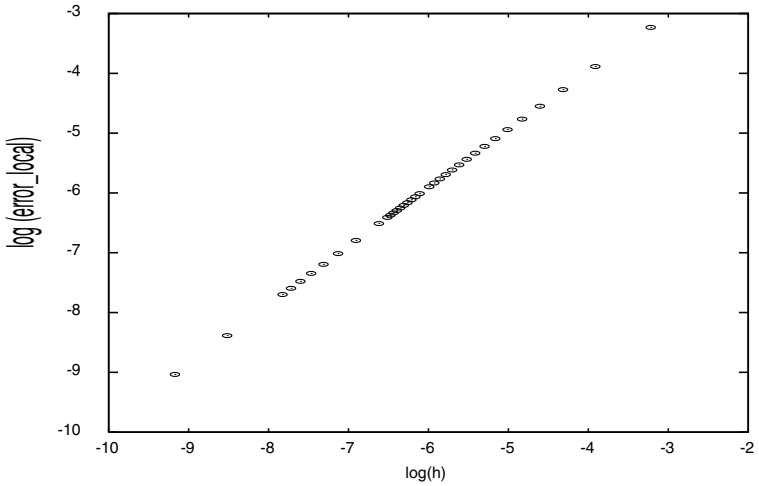

Fig. 6. The local maximum error around the sonic point versus the space size in a log scale for the Burger's equation.

write Eq. (2.1) and the Godunov scheme in a non-conservative form, respectively. Using the Godunov scheme, we have

$$u_j^{n+1} = \begin{cases} \frac{-x_j}{t_n} + \sigma \frac{-x_j - x_{j-1}}{2t_n} \left(\frac{-x_{j-1}}{t_n} - \frac{-x_j}{t_n} \right) & \text{for } x \in (x_L, 0), \\ \frac{-x_j}{t_n} + \sigma \frac{-x_j - x_{j+1}}{2t_n} \left(\frac{-x_j}{t_n} - \frac{-x_{j+1}}{t_n} \right) & \text{for } x \in (0, x_R). \end{cases} \tag{2.21}$$

Due to the upwind flux at a cell interface, the numerical wave propagation speed at x_j becomes $(-x_j - x_{j-1})/2t_n$ for $x_j < -h$ and $(-x_j - x_{j+1})/2t_n$ for $x_j > h$. Comparing them with the exact wave speed $-x_j/t_n$, we can find that the numerical wave speeds are faster than the exact wave speeds in both regions, that is to say, $(-x_j - x_{j-1})/2t_n > -x_j/t_n > 0$ in the region $(x_L, -h)$ and $0 > -x_j/t_n > (-x_j - x_{j+1})/2t_n$ in the region (h, x_R). Thus, the propagation of the approximate solution undergoes a advance around the sonic point and the

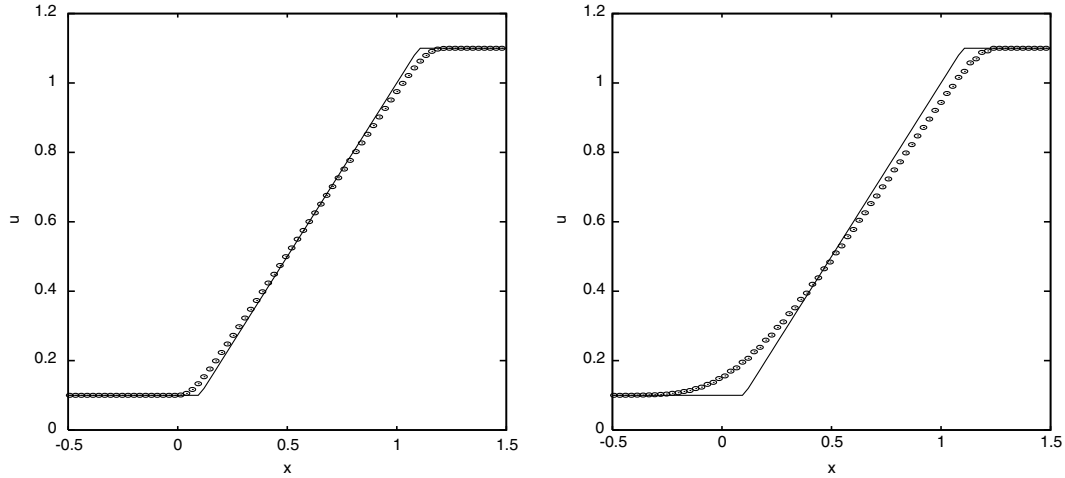

Fig. 7. The supersonic solutions ("circle") of the Burgers' equation at $t = 0.9$ are computed by using the Godunov method (left) and the LxF scheme (right) with 150 grid cells and $t_n = 0.1$ for $u_L = 0.1$ and $u_R = 1.1$. The solid line denotes the exact solution.

compression is accelerated. Due to it, the discontinuous jump around the sonic point cannot be observed in a transonic compression region. For comparison, we show wave propagation speeds for the sonic compression and rarefaction waves in Fig. 8, where the solid and dotted lines denote the exact and numerical wave propagation speeds, respectively.

2.2. The central-difference schemes

As we have known, for most upwind schemes, the numerical dissipation goes to a minimum value around the sonic point [6]. *Is the sonic glitch formed due to a smaller numerical viscosity or any upwind scheme*? To answer this question, we check the value of u_j^{n+1} calculated by using the LxF scheme and the Lax–Wendroff (LW) scheme. The LxF scheme is of a relatively large numerical viscosity, while the LW scheme is of a smaller viscosity than that of the Godunov scheme. For the LxF scheme, the update of the variable u_j^{n+1} is

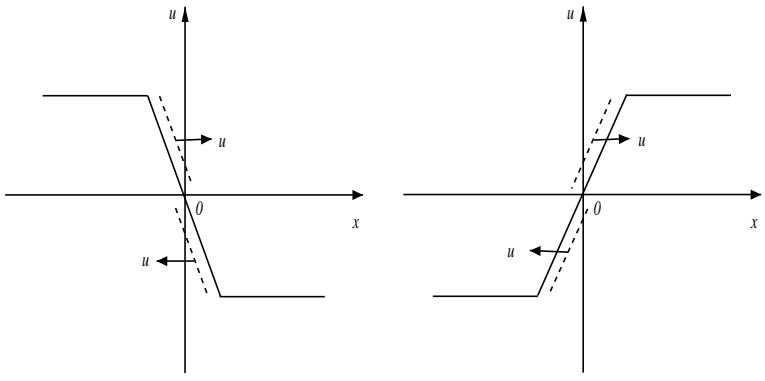

Fig. 8. The wave propagation speeds. Left: a sonic compression wave; right: a sonic rarefaction wave.

$$u_j^{n+1} = \frac{1}{2}\left(u_{j+1}^n + u_{j-1}^n\right) + \frac{\sigma}{2}\left(f(u_{j-1}^n) - f(u_{j+1}^n)\right)$$
$$= \frac{1}{2}\left(\frac{x_{j+1}}{t_n} + \frac{x_{j-1}}{t_n}\right) + \frac{\sigma}{2}\left(\frac{1}{2}\left(\frac{x_{j-1}}{t_n}\right)^2 - \frac{1}{2}\left(\frac{x_{j+1}}{t_n}\right)^2\right) = \frac{x_j}{t_n}\left(1 - \frac{\tau}{t_n}\right) = u_j^{\mathrm{e}} + \mathcal{O}(\tau^2), \tag{2.22}$$

in the region $t_n - h > x_j > -t_n + h$. It is worth noting that the variable u_j^{n+1} calculated by the unstable central scheme:

$$u_j^{n+1} = u_j^n + \frac{\sigma}{2}\left(f(u_{j-1}^n) - f(u_{j+1}^n)\right)$$

equals to $(x_j/t_n)(1 - \tau/t_n)$ too, although its numerical viscosity is zero. Moreover, the gradients of their solutions equal to $(1 - \tau/t_n)/t_n$ within the rarefaction wave region that is a second-order accurate approximation to the exact one in time. If let $\tau \to 0$, then the gradient of the numerical solution computed by the LxF scheme should tend to the gradient of the exact solution at any time $t > t_n$.

For the Godunov scheme, from (2.15) and (2.16), we may derive the approximate gradient at $t = t_n + \tau$ within the rarefaction fan as follows:

$$\frac{u_{j+1}^{n+1} - u_j^{n+1}}{h} = \begin{cases} \frac{1}{t_n+\tau} + \widetilde{C}\tau + \mathcal{O}(\tau^2), & \text{near the sonic point,} \\ \frac{1}{t_n+\tau} + \mathcal{O}(\tau^2), & \text{otherwise,} \end{cases}$$

where $\widetilde{C} = \mathcal{O}(1)$. Therefore, the approximate gradient at $t = T \equiv t_n + N\tau$ within the rarefaction fan becomes

$$\frac{u_{j+1}^{n+N} - u_j^{n+N}}{h} = \begin{cases} \frac{1}{T} + \mathcal{O}(1) + \mathcal{O}(\tau), & \text{near the sonic point,} \\ \frac{1}{T} + \mathcal{O}(\tau), & \text{otherwise,} \end{cases}$$

or

$$\lim_{\tau,h\to 0} \frac{u_{j+1}^{n+N} - u_j^{n+N}}{h} = \begin{cases} \frac{1}{T} + \mathcal{O}(1), & \text{near the sonic point,} \\ \frac{1}{T}, & \text{otherwise,} \end{cases}$$

where $\mathcal{O}(1)$ depends on T or N, but does not on the cell number. In Fig. 9, we show the gradients of the numerical and exact solutions for the sonic rarefaction problem. The numerical solutions are computed by two difference schemes, the LxF scheme with 10,000 cells and the Godunov scheme with 10,000 cells as well as 38,440 cells. These numerical results coincide with the above theoretical results.

Similarly, the variable u_j^{n+1} can also be updated by using the LW scheme as

$$u_j^{n+1} = u_j^n + \frac{\sigma}{2}\left(f(u_{j-1}^n) - f(u_{j+1}^n)\right) + \frac{\left(\sigma a(u_{j+\frac{1}{2}})\right)^2}{2}\left(u_{j+1}^n - u_j^n\right) - \frac{\left(\sigma a(u_{j-\frac{1}{2}})\right)^2}{2}\left(u_j^n - u_{j-1}^n\right)$$
$$= \frac{x_j}{t_n} + \frac{\sigma}{2}\left(\frac{1}{2}\left(\frac{x_{j-1}}{t_n}\right)^2 - \frac{1}{2}\left(\frac{x_{j+1}}{t_n}\right)^2\right) + \frac{\sigma^2\left(u_{j+1}^n + u_j^n\right)^2}{8}\left(\frac{x_{j+1}}{t_n} - \frac{x_j}{t_n}\right) - \frac{\sigma^2\left(u_j^n + u_{j-1}^n\right)^2}{8}\left(\frac{x_j}{t_n} - \frac{x_{j-1}}{t_n}\right)$$
$$= \frac{x_j}{t_n}\left(1 - \frac{\tau}{t_n} + \left(\frac{\tau}{t_n}\right)^2\right) = u_j^{\mathrm{e}} + \mathcal{O}(\tau^3), \tag{2.23}$$

in both region $t_n - h > x_j > -t_n + h$. From (2.22) and (2.23), it is not difficult to find that there is neither additional term $\tau h/2t_n^2$, nor the sonic glitch. The gradient of the solution of the LW scheme equals to $(1 - (\tau/t_n) + (\tau/t_n)_2)/t_n$ within the rarefaction wave region that is a third-order accurate approximation to the exact one in time. When $\tau \to 0$, it should tend to the gradient of the exact solution too. The numerical solutions shown in Fig. 10 are consistent with this theoretical analysis. They are obtained by using the LxF

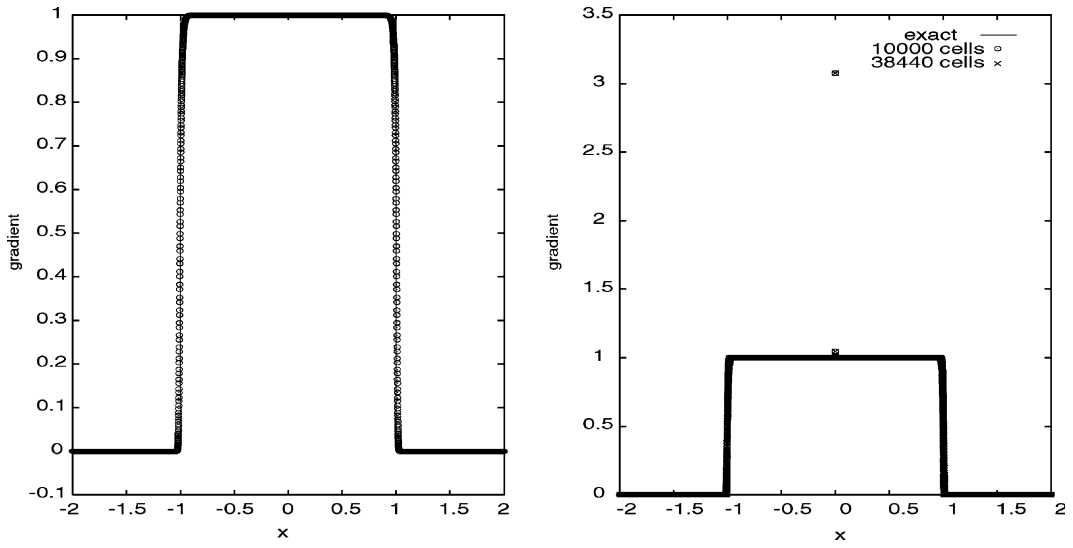

Fig. 9. The gradients of the numerical solutions for the sonic rarefaction problem computed by using the LxF scheme with 10,000 cells (left) and the Godunov scheme with 10,000 cells as well as 38,440 cells.

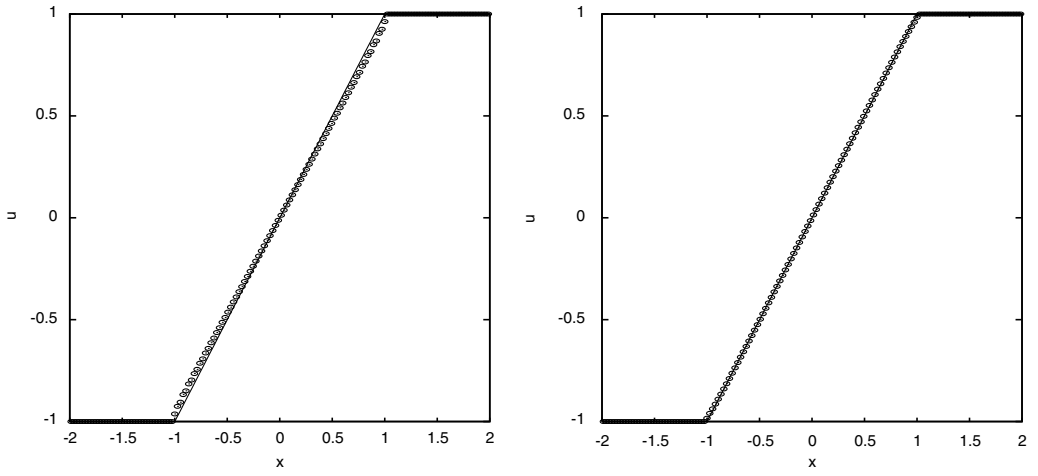

Fig. 10. Same as Fig. 3, except for the LxF scheme (left) and the LW scheme (right), respectively.

scheme (left) and the LW scheme (right), respectively. From Fig. 11, we may observe that there is no local extremum in the actual error profile near the sonic point.

2.3. The other schemes

We may further show that the glitch is closely associated with the upwind flux, even though the numerical viscosity is big enough. Consider a general three-point scheme

$$u_j^{n+1} = u_j^n + \frac{\sigma}{2}\left(f(u_{j-1}^n) - f(u_{j+1}^n)\right) + \frac{Q(v_{j+\frac{1}{2}})}{2}\left(u_{j+1}^n - u_j^n\right) - \frac{Q(v_{j-\frac{1}{2}})}{2}\left(u_j^n - u_{j-1}^n\right), \tag{2.24}$$

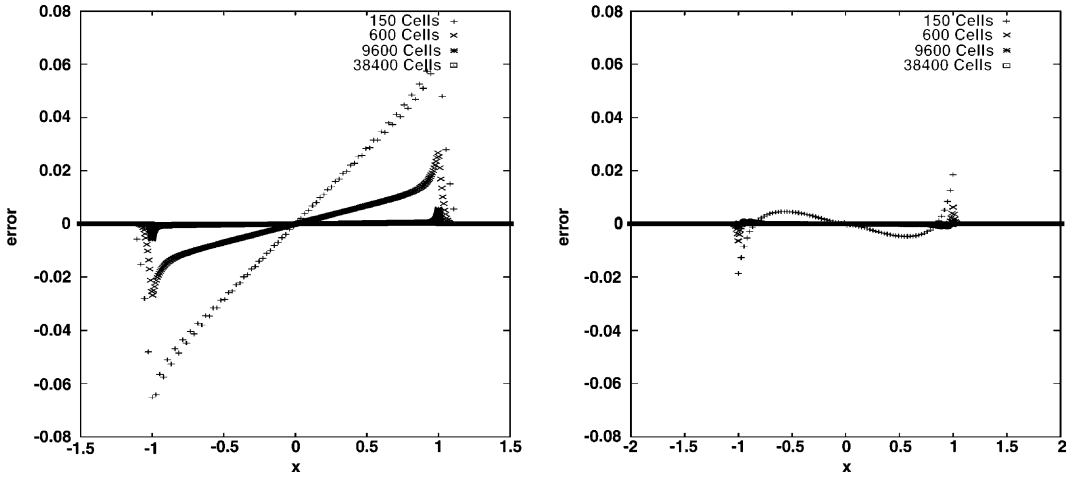

Fig. 11. Same as Fig. 5, except for the LxF scheme (left) and the LW scheme (right), respectively.

where $Q_{j+\frac{1}{2}} = Q(v_{j+\frac{1}{2}})$ is usually referred as numerical viscosity, $v = \sigma a$. According to the above analysis, if we take $Q_{j+\frac{1}{2}} = \frac{1}{2}(Q^{G}_{j+\frac{1}{2}} + Q^{L}_{j+\frac{1}{2}})$ or $\frac{1}{2}(Q^{R}_{j+\frac{1}{2}} + Q^{L}_{j+\frac{1}{2}})$, then a shift, $\tau h/2(t_n)^2$, will be also formed when the variable u^{n+1}_j is updated, where $Q^{G}_{j+\frac{1}{2}}$, $Q^{R}_{j+\frac{1}{2}}$, and $Q^{L}_{j+\frac{1}{2}}$ denote the numerical viscosities of the Godunov method, the Roe scheme, and the LxF scheme, respectively. We have used these two weighted average schemes to solve the above problem with same grid points and parameters. Fig. 12 only show close-up of the solutions and error given by the weighted average scheme with $Q = \frac{1}{2}(Q^{R} + Q^{L})$. Although the error around the sonic point is very small and almost invisible, local extrema still exist and the solution is not monotone with respect to x/t along the transonic expansion fan.

In the literature, to cure the sonic glitch, an entropy fix is usually added to modify numerical viscosity of a finite-difference scheme, see e.g. [27]. For the traditional upwind scheme, we may use Harten's entropy fix [5], i.e.,

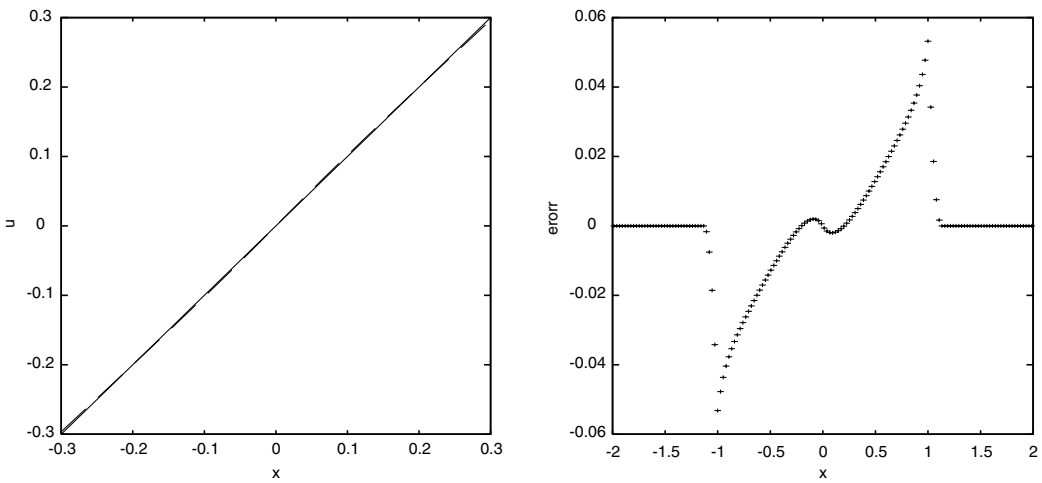

Fig. 12. Close-up of the computed solution (left) and error (right) for the Burgers' equation are calculated by using the weighted average scheme with $Q = \frac{1}{2}(Q^{R} + Q^{L})$.

$$Q(x) = \begin{cases} |x| & \text{if } |x| > \epsilon, \\ \frac{x^2+\epsilon^2}{2\epsilon} & \text{if } |x| \leqslant \epsilon, \end{cases} \tag{2.25}$$

where ϵ is a given positive constant. In fact, after doing that, it is seen that the numerical viscosity of the scheme does not depend on the characteristic direction if $|x| \leqslant \epsilon$. But, there still exists the shift between the approximate solution and the "exact" solution if $t_n - h > |x| > \epsilon + h$. In other words, we can smear out the non-physical jump or give a smooth transition around the sonic point by adding an entropy fix, but the error within the sonic rarefaction wave cannot be completely eliminated in theory, except that the parameter ϵ is big enough such that $\epsilon + h \geqslant t_n - h$. It means that the error around the sonic point may become (almost) invisible, if we take a relatively large ϵ. But, resolution of the tail and head of the rarefaction wave will also be decreased. Moreover, numerical solutions will also suffer possibly a loss of monotonicity with respect to x/t along the rarefaction waves. To demonstrate it, in Figs. 13–15, we give the numerical solutions, corresponding errors, and the gradients of the numerical solutions calculated by using the Roe scheme with the entropy fix (2.25) for $\epsilon = 0.1$ (left) and $\epsilon = 0.5$ (right), respectively. Obviously, the numerical solutions with an entropy fix have been improved in comparison with one in Fig. 4, in particular, the error around the sonic point is almost invisible in the case of $\epsilon = 0.5$. But numerical dissipation of the scheme has also become larger than one in Fig. 4 such that resolution of the tail and head of the rarefaction waves is decreased. We refer the reader to compare our error plots in Figs. 5 and 14, and figures given in [24] as well as Section 3 for more computations.

Finally, we consider evolution of the transonic expansion fan by using the MUSCL scheme of van Leer [25] and the TVD scheme of Harten [5].

Under our assumption, the MUSCL scheme advances the solution via the equation

$$u_j^{n+1} = u_j^n - \sigma\left(\hat{f}(u_{j+\frac{1}{2}}^{n,\mathrm{L}}, u_{j+\frac{1}{2}}^{n,\mathrm{R}}) - \hat{f}(u_{j-\frac{1}{2}}^{n,\mathrm{L}}, u_{j-\frac{1}{2}}^{n,\mathrm{R}})\right),$$

$$u_{j+\frac{1}{2}}^{n,\mathrm{L}} = u_j^n + \frac{h}{2}S_j^n, \quad u_{j+\frac{1}{2}}^{n,\mathrm{R}} = u_{j+1}^n - \frac{h}{2}S_{j+1}^n,$$

where $\hat{f}_{j+\frac{1}{2}}$ is any numerical flux of three-point conservative schemes, and $S_j^n \approx \partial u/\partial x$. Here, we take $\hat{f}_{j+\frac{1}{2}}$ as the numerical flux of the Godunov scheme and S_j^n is defined by

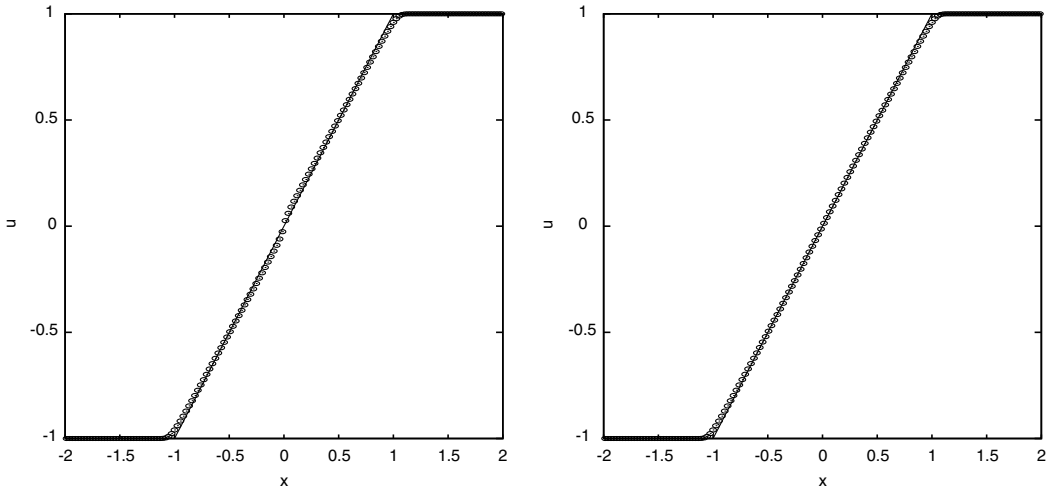

Fig. 13. Same as Fig. 4, except with an entropy fix. Left: $\epsilon = 0.1$; right: $\epsilon = 0.5$.

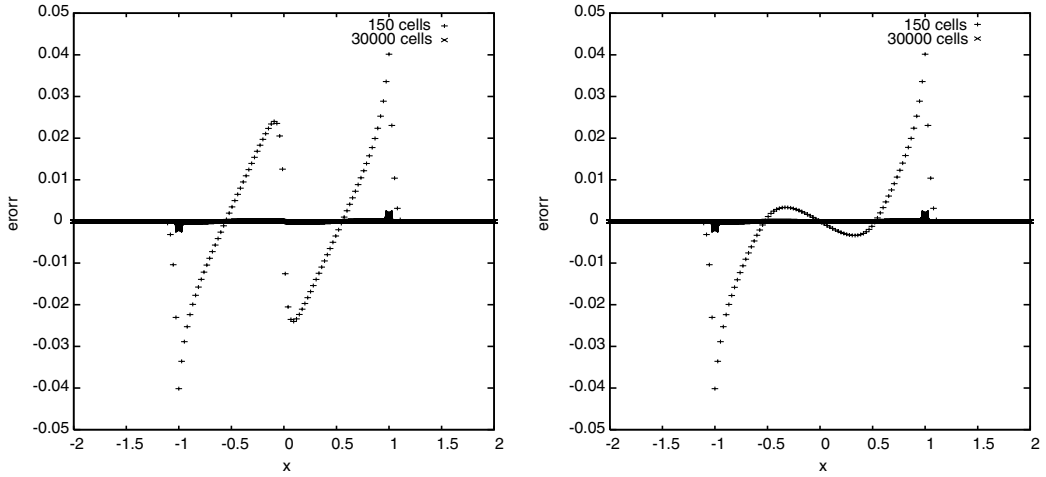

Fig. 14. The numerical errors corresponding to Fig. 13. Left: $\epsilon = 0.1$; right: $\epsilon = 0.5$.

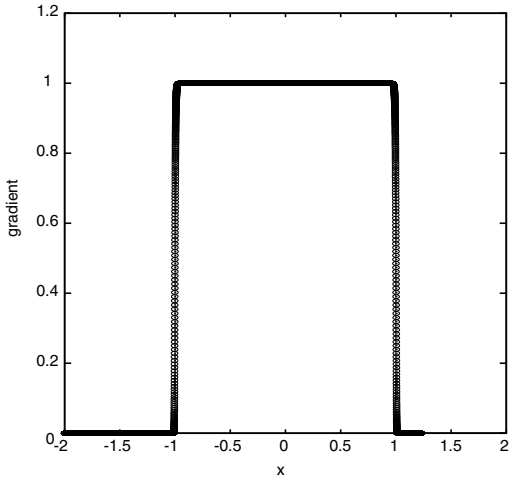

$$S_j^n = \begin{cases} \frac{1}{h} s_{j+\frac{1}{2}} \min\{s_{j+\frac{1}{2}}(u_j - u_{j-1}), |u_{j+1} - u_j|\} & \text{if } (u_j - u_j - 1)(u_{j+1} - u_j) > 0, \\ 0 & \text{otherwise,} \end{cases}$$

where $s_{j+\frac{1}{2}} = \text{sign}(u_j + 1 - u_j)$. Within the rarefaction fan away from its two corners, we have

$$S_j^n = \frac{1}{t_n}.$$

Hence, (2.15) and (2.16) are replaced by

$$u_j^{n+1} = \frac{x_j}{t_n} + \sigma\left(\frac{1}{2}\left(\frac{x_{j-1}}{t_n} + \frac{h}{2t_n}\right)^2 - \frac{1}{2}\left(\frac{x_j}{t_n} + \frac{h}{2t_n}\right)^2\right) = \widetilde{u}_j^{\text{e}}, \tag{2.26}$$

and

$$u_j^{n+1} = \frac{x_j}{t_n} + \sigma\left(\frac{1}{2}\left(\frac{x_j}{t_n} - \frac{h}{2t_n}\right)^2 - \frac{1}{2}\left(\frac{x_{j+1}}{t_n} - \frac{h}{2t_n}\right)^2\right) = \widetilde{u}_j^{\mathrm{e}}, \tag{2.27}$$

respectively. It is very obvious that the additional terms in (2.15) and (2.16) have been eliminated. In fact, the numerical viscosity terms in the MUSCL scheme approximate the Burgers' equation have become zero within the transonic expansion fan now. The actual error of the MUSCL scheme is presented in Fig. 16. We can find that local maximum of $|u_j^{n+1} - u_j^{\mathrm{e}}|$ is only located at two corners of the rarefaction wave.

The Harten TVD scheme for the inviscid Burgers' equation can be written as follows:

$$u_j^{n+1} = u_j^n - \sigma\left(\hat{f}_{j+\frac{1}{2}}^n - \hat{f}_{j-\frac{1}{2}}^n\right), \tag{2.28}$$

where $\hat{f}_{j+\frac{1}{2}}$ is defined by

$$\begin{aligned}
&\hat{f}_{j+\frac{1}{2}} = \frac{1}{2}\left(f(u_j) + f(u_{j+1}) + g_j + g_{j+1} - |a(u) + \gamma|_{j+\frac{1}{2}}(u_{j+1} - u_j)\right),\\
&g_j = s_{j+\frac{1}{2}} \min\{s_{j+\frac{1}{2}}\widetilde{g}_{j-\frac{1}{2}}, |\widetilde{g}_{j+\frac{1}{2}}|\}, \quad s_{j+\frac{1}{2}} = \mathrm{sign}(\widetilde{g}_{j+\frac{1}{2}}),\\
&\widetilde{g}_{j+\frac{1}{2}} = \frac{1}{2}\left(|a(u)| - \sigma a(u)^2\right)_{j+\frac{1}{2}}(u_{j+1} - u_j),\\
&\gamma_{j+\frac{1}{2}} = \begin{cases} (g_{j+1} - g_j)/(u_{j+1} - u_j), & u_{j+1} \neq u_j,\\ 0, & u_{j+1} = u_j. \end{cases}
\end{aligned}$$

Within the rarefaction fan away from its two corners, we have

$$g_j = \frac{h}{2\sigma t_n} \min\left\{(|\sigma u| - (\sigma u)^2)_{j+\frac{1}{2}}, (|\sigma u| - (\sigma u)^2)_{j-\frac{1}{2}}\right\},$$

which depends strongly on the characteristic direction and is highly nonlinear. Thanks to this, it is difficult to give exactly a simple representation of the solution u_j^{n+1}. Here, we only plot the computed error $u_j^{n+1} - u_j^{\mathrm{e}}$ in Fig. 16. The sonic glitch has been formed by the TVD scheme of Harten.

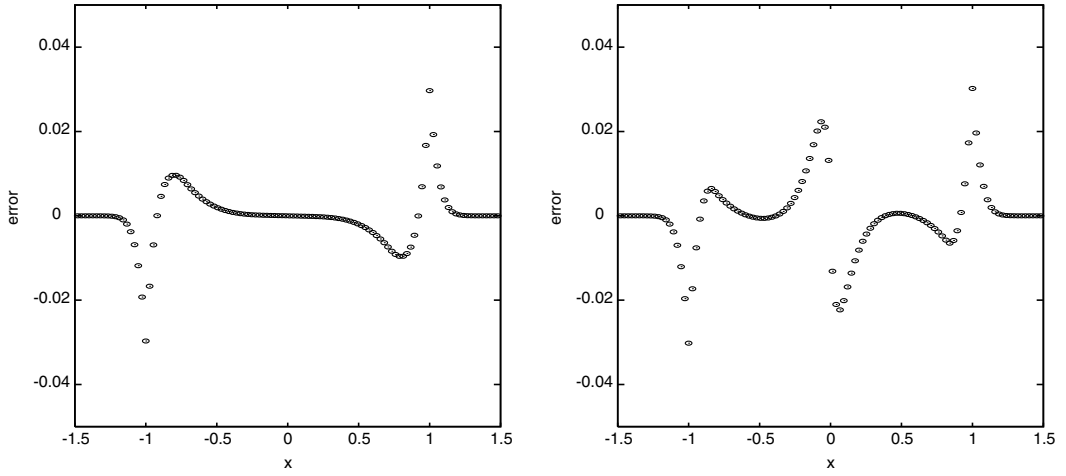

Fig. 16. Same as Fig. 4, except for the MUSCL scheme of van Leer (left) and the Harten TVD scheme [5] (right).

From the above analysis, we can conclude that the sonic glitch is not left from any initial discontinuous data of a shock tube problem. Even started from the continuous exact rarefaction wave, a glitch can still be formed. The sonic glitch affects the upwind flux and not the central-difference method, such as the LxF scheme and the LW scheme as well as the central scheme with zero viscosity, because they do not depend on the characteristic direction. The sonic glitch has no any direct connection with the violation of the entropy condition or the size of numerical viscosity of a finite-difference scheme. Glitch may also be formed by several "good" schemes, such as the Godunov scheme and the Engquist–Osher scheme as well as the high resolution scheme of Harten. The sonic glitch is mainly coming from the disparity wave speeds across the sonic point in a transonic expansion fan. If a viscous governing equation is solved by a central-difference scheme, there will not have a clear upwind wave propagation direction at a cell interface; and we may expect that the glitch is not formed. A suitable entropy fix can be used to give a smooth transition around the sonic point, but the disparity wave speeds are still existing generally and it will decrease resolution of two corners of rarefaction wave. The initial data reconstruction technique of van Leer can be used to eliminate the sonic glitch when we solve the inviscid Burgers' equation.

3. The sonic glitch in the Euler equations

In this section we begin to analyze rarefaction wave in the Euler equations

$$\frac{\partial U}{\partial t}+\frac{\partial F(U)}{\partial x}=0, \tag{3.1}$$

where

$$U=[\rho,\rho u,E]^{\mathrm{T}},\quad F(U)=[\rho u,\rho u^2+p,u(E+p)]^{\mathrm{T}}. \tag{3.2}$$

Here ρ is the fluid density, u is the velocity, p is the pressure and E denotes the total energy. To close this system, we need an equation of state to relate the pressure to the total energy:

$$p=(\gamma-1)\left(E-\frac{1}{2}\rho u^2\right),$$

where γ denotes the ratio of the specific heats. The Jacobian matrix $A(U)=\partial F(U)/\partial U$ has three real eigenvalues:

$$\lambda_1=u-a,\quad \lambda_2=u,\quad \lambda_3=u+a,$$

where a denotes the sound speed, $a=\sqrt{\gamma p/\rho}$.

In the following, we will solve the Toro's shock tube problem for a perfect gas with $\gamma=1.4$ and initial data

$$(\rho,u,p)(x,0)=\begin{cases}(1,0.75,1), & x<0.3,\\ (0.125,0,0.1), & x>0.3.\end{cases} \tag{3.3}$$

For this standard shock tube problem, the Godunov method generates clearly a sonic glitch at the left running rarefaction wave around the sonic point $x=x_0\equiv 0.3$, where $\lambda_1=0$. The numerical solutions calculated by the Godunov method are shown in Fig. 17. We also refer the reader to [24] for more computed results. The reason for the glitch formation in the Euler solution is basically same as that in the Burgers' equation, but the theoretical analysis is more complex because there are three characteristic directions at each point (x,t). In the following, we can only give a mimic analysis. For the above shock tube problem, the left running rarefaction wave is constructed by the characteristic wave with speed $\lambda_1=u-a$. For this wave, the exact solution of the velocity field u is a similarity solution (see e.g. [24, p. 135], as well as [1])

$$u(x,t) = \frac{2}{\gamma+1}\left(a_{\mathrm{L}} + \frac{\gamma-1}{2}u_{\mathrm{L}} + \frac{x-x_0}{t}\right), \tag{3.4}$$

where a_{L} is the sound speed computed according to the initial left state. The exact sound speed is

$$a(x,t) = \frac{2}{\gamma+1}\left(a_{\mathrm{L}} + \frac{\gamma-1}{2}\left(u_{\mathrm{L}} - \frac{x-x_0}{t}\right)\right).$$

Therefore, similar to the Burgers' equation, the characteristic wave speed λ_1 in the left rarefaction wave equals to:

$$\lambda_1 = u(x,t) - a(x,t) = \frac{x-x_0}{t}. \tag{3.5}$$

To clarify the problem, we use the Steger–Warming (S–W) FVS scheme and the Roe scheme as two examples. The S–W FVS scheme satisfies the following proposition [22].

Proposition 3.1. *The macroscopic conservative variables* $U = [\rho, \rho u, E]^T$ *and the associated split flux component* $F^{\pm}$ *in the Steger–Warming FVS scheme can be written as follows*:

$$U = \sum_{k=1}^{3} U^{(k)}, \quad F^{\pm}(U) = \sum_{k=1}^{3} F^{(k),\pm}(U), \quad F^{(k),\pm}(U) = \sum_{k=1}^{3} \lambda_k^{\pm} U^{(k)}, \tag{3.6}$$

where

$$U^{(2)} = \frac{\gamma-1}{\gamma}\begin{pmatrix} \rho \\ \rho\lambda_2 \\ \frac{1}{2}\rho(\lambda_2)^2 \end{pmatrix}, \quad U^{(k)} = \frac{1}{2\gamma}\begin{pmatrix} \rho \\ \rho\lambda_k \\ \frac{1}{2}\rho(\lambda_k)^2 + \frac{\gamma(3-\gamma)}{2}\rho e \end{pmatrix}, \quad k = 1 \text{ or } 3. \tag{3.7}$$

Here, $\lambda_k^{\pm} = \frac{1}{2}(\lambda_k \pm |\lambda_k|)$.

This proposition shows that the flow inside each cell can be considered as consisting of three particles and each one is associated with its individual mass, momentum, and the energy, i.e. $U^{(k)}$. Their speeds are λ_k, $k = 1, 2, 3$, respectively. The fluxes are equal to the particle variable $U^{(k)}$ multiplied by the corresponding particle velocity.

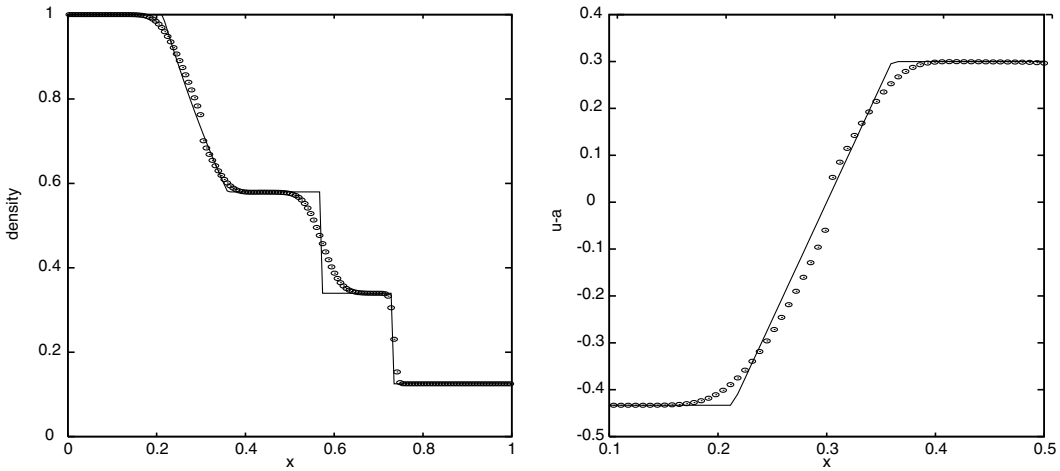

Fig. 17. The computed solutions ("circle") of the Euler equations are given by using the Godunov method and 150 grid cells. The solid line denotes the exact solution. Left: the density distribution; right: the characteristic wave speed $u - a$ in the rarefaction wave.

Since the characteristic wave speed λ_1 is linearly distributed with respect to $(x - x_0)/t$ in the rarefaction wave, see Eq. (3.5), after numerical discretization at a cell interface the wave propagation speed of the Riemann solver becomes

$$(\lambda_1)^n_{j+\frac{1}{2}} = \begin{cases} (\lambda_1)_j \equiv \left(\frac{x_j - x_0}{t}\right), & \text{in the supersonic region } u > a, \\ (\lambda_1)_{j+1} \equiv \left(\frac{x_{j+1} - x_0}{t}\right), & \text{in the subsonic region } u < a, \end{cases} \tag{3.8}$$

and the flux $F^{(1)} = F^{(1),+} + F^{(1),-}$ in the vicinity of the first rarefaction wave is approximated as

$$F^{(1)}_{j+\frac{1}{2}} \approx \begin{cases} \left(\frac{x_j - x_0}{t}\right) U^{(k)}_j, & \text{in the supersonic region } u > a, \\ \left(\frac{x_{j+1} - x_0}{t}\right) U^{(k)}_{j+1}, & \text{in the subsonic region } u < a. \end{cases} \tag{3.9}$$

Hence, the magnitude of the numerical wave speed at a cell interface $x_{j+\frac{1}{2}}$ is smaller than the exact one, $(\lambda_1)^e = ((x_{j+\frac{1}{2}} - x_0)/t)$, in both the supersonic and subsonic regions. The velocity difference $(\lambda_1)^n_{j+\frac{1}{2}} - (\lambda_1)^e_{j+\frac{1}{2}}$ will be proportional to h in both regions. As a result, the sonic glitch will be formed around the sonic point $x = x_0$, where $u = a$. The disparity in the characteristic wave speed λ_1 is clearly demonstrated in the right picture of Fig. 17, where the numerical distribution $u - a$ is above the exact solution in the supersonic side, $x > x_0$, and below the exact one in the subsonic side, $x < x_0$, which is similar to that of the Burgers' equation. According to the above analysis, we can expect that if using the "exact" wave speed $(\lambda_1)^e_{j+\frac{1}{2}}$ to replace the approximate one given in (3.8), then we may give an improved solution around the sonic point. To validate it, we compute the Toro's shock tube problem by using the Steger–Warming FVS scheme and its modified version. The profiles of the density and the error, $(\lambda_1)_{j+\frac{1}{2}} - (\lambda_1)^e_{j+\frac{1}{2}}$, are shown in Figs. 18 and 19, respectively. Comparing them, we can find that the error around the sonic point is efficiently reduced by using the "exact" wave speed.

Remark 3.1. It is worth noting that in the above computations we only modify the characteristic wave speed λ_1, i.e. define $(\lambda_1)_{j+\frac{1}{2}} = \frac{1}{2}((\lambda_1)_{j+1} + (\lambda_1)_j)$. In practice it seems not be very efficient for a general problem, especially for a multi-dimensional problem. However, if the values of the three characteristic speeds are all defined exactly, i.e. $(\lambda_k)_{j+\frac{1}{2}} = \frac{1}{2}((\lambda_k)_{j+1} + (\lambda_k)_j)$ $k = 1, 2, 3$, then it is possible to give oscillation or overshoot near the shock wave when the CFL number is large. We have checked that the overshoot may be avoided for the Toro's problem when the CFL number is less than 0.5.

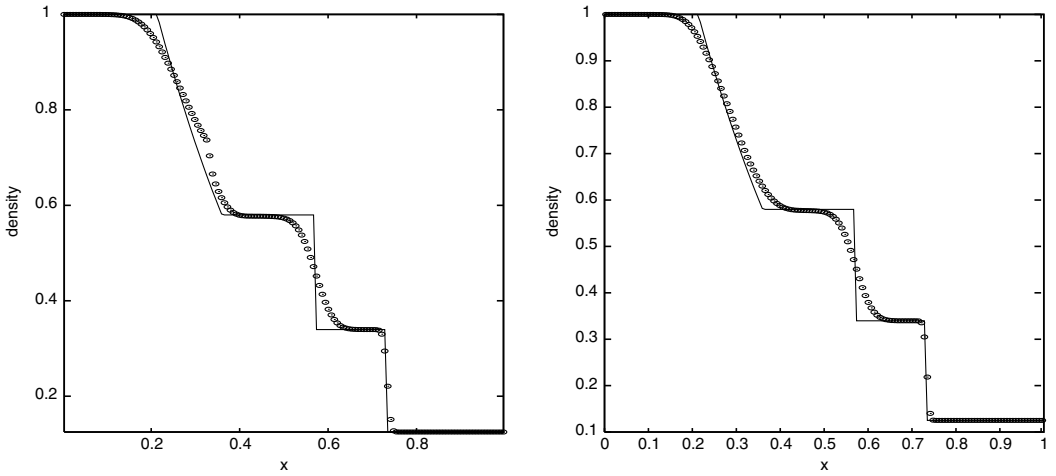

Fig. 18. Same as Fig. 17, except for the original S–W FVS scheme (left) and the modified S–W FVS scheme (right).

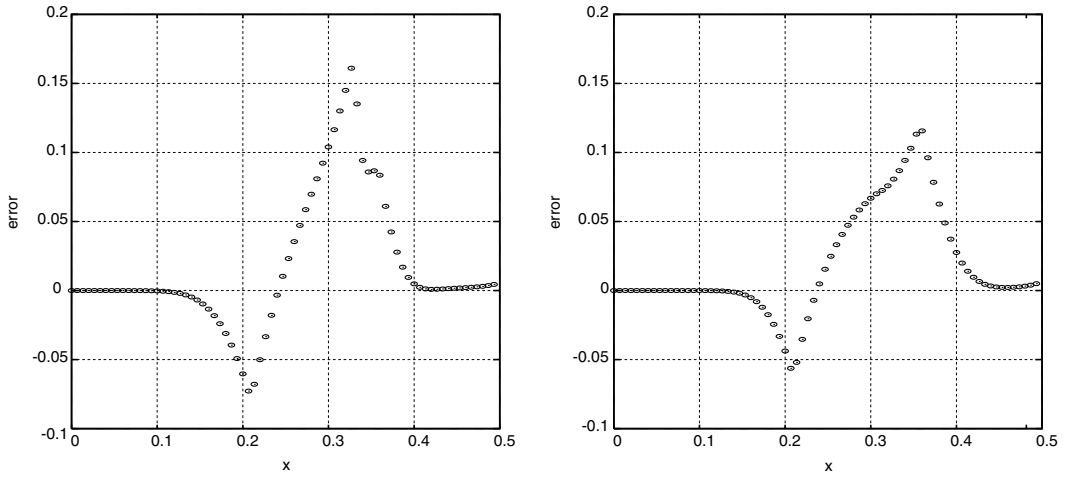

Fig. 19. Close-up of the error, $(\lambda_1)_{j+\frac{1}{2}} - (\lambda_1)^{e}_{j+\frac{1}{2}}$, for the S–W FVS scheme (left) and the modified S–W FVS scheme (right).

The Roe scheme for the Euler equation can be described as follows [17,24]:

$$U_j^{n+1} = U_j^n - \sigma\left(\hat{F}^n_{j+\frac{1}{2}} - \hat{F}^n_{j-\frac{1}{2}}\right), \tag{3.10}$$

where the numerical flux $\hat{F}^n_{j+\frac{1}{2}}$ is calculated

$$\hat{F}_{j+\frac{1}{2}} = \frac{1}{2}\left(F(U_j) + F(U_{j+1}) - \sum_{k=1}^{3} \alpha^{(k)}_{j+\frac{1}{2}} |(\lambda_k)_{j+\frac{1}{2}}| R^{(k)}_{j+\frac{1}{2}}\right),$$

where $R^{(1)}$, $R^{(2)}$ and $R^{(3)}$ are corresponding right eigenvectors, i.e.

$$R^{(2)} = \frac{\gamma}{\rho(\gamma-1)} U^{(2)}, \quad R^{(k)} = \frac{2\gamma}{\rho} U^{(k)}, \quad k = 1 \text{ or } 3,$$

and the wave strengths $\alpha^{(k)}_{j+\frac{1}{2}}$ satisfy

$$U_{j+1} - U_j = \sum_{k=1}^{3} \alpha^{(k)}_{j+\frac{1}{2}} R^{(k)}_{j+\frac{1}{2}}.$$

Thanks to the identity $F(U_{j+1}) - F(U_j) = \widetilde{A}^{\mathrm{Roe}}(U_{j+1}, U_j)(U_{j+1} - U_j)$, the Roe scheme (3.10) can be rewritten in a non-conservative form

$$U_j^{n+1} = U_j^n - \sigma \sum_{k=1}^{3} \left((\lambda_k^-)_{j+\frac{1}{2}} \alpha^{(k)}_{j+\frac{1}{2}} R^{(k)}_{j+\frac{1}{2}} + (\lambda_k^+)_{j-\frac{1}{2}} \alpha^{(k)}_{j-\frac{1}{2}} R^{(k)}_{j-\frac{1}{2}}\right).$$

It means that the solution U_j^{n+1} is updated via propagation of three waves with their individual speeds $(\lambda_k^-)_{j+\frac{1}{2}}$ or $(\lambda_k^+)_{j-\frac{1}{2}}$, $k = 1, 2, 3$. Because the actual wave speed at (x_j, t_n) should be $(\lambda_k^-)_j$ or $(\lambda_k^+)_j$, the magnitude of the numerical wave speed at x_j is smaller than the exact one, $(\lambda_1)^{e} = ((x_j - x_0)/t)$, in both the supersonic and subsonic regions, and the sonic glitch cannot be avoided.

Finally, we conduct some numerical experiments to check if the upwind scheme with an entropy fix, the MUSCL method of van Leer, and the Harten high resolution scheme influence individually computation of the sonic rarefaction wave in the Euler equations. For the Euler equations, we cannot strictly prove the fact that the MUSCL method can fully eliminate the sonic glitch around the sonic point, but we may expect that

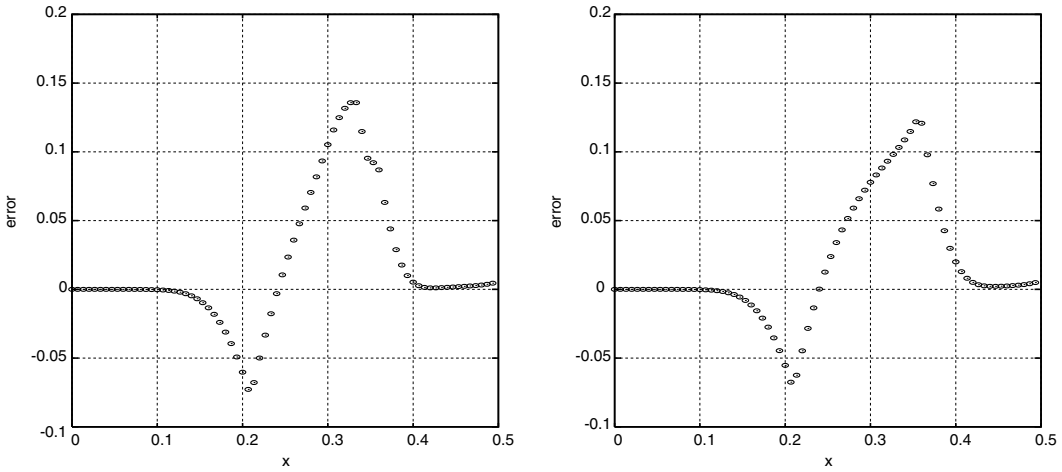

Fig. 20. Same as Fig. 19, except for the S–W FVS scheme with an entropy fix. Left: $\epsilon = 0.1$; right: $\epsilon = 0.5$.

it can efficiently reduce the numerical error. We calculate the Toro's problem by the Roe scheme with the entropy fix (2.25) for $\epsilon = 0$, 0.1, 0.2, and 0.3, respectively. The results are shown in Figs. 21 and 22. Similar to the case of the Burgers' equation, with an entropy fix, we may smear out the jump or give a smooth transition around the sonic point with a large ϵ, but there still exists a small numerical error within the sonic rarefaction waves. Moreover, the numerical solutions shown in Figs. 21 and 22 are not monotone with respect to $(x - x_0)/t$ along the rarefaction waves. In Fig. 23, we show the density and characteristic speed λ_1 calculated by using the MUSCL scheme with the Roe approximate solver and the minmod limiter for the approximate slope. In our computations, the reconstruction is implemented on the conservative variables. In Fig. 24, we give the numerical solutions of the Toro's problem calculated by the Harten UNO scheme combining the Roe approximate solver with an entropy fix. These results show that the flaw around the sonic point has been efficiently reduced by using high resolution schemes. In Fig. 20, we also give close-up of the error for the SW FVS scheme with an entropy fix comparing to ones in Fig. 19.

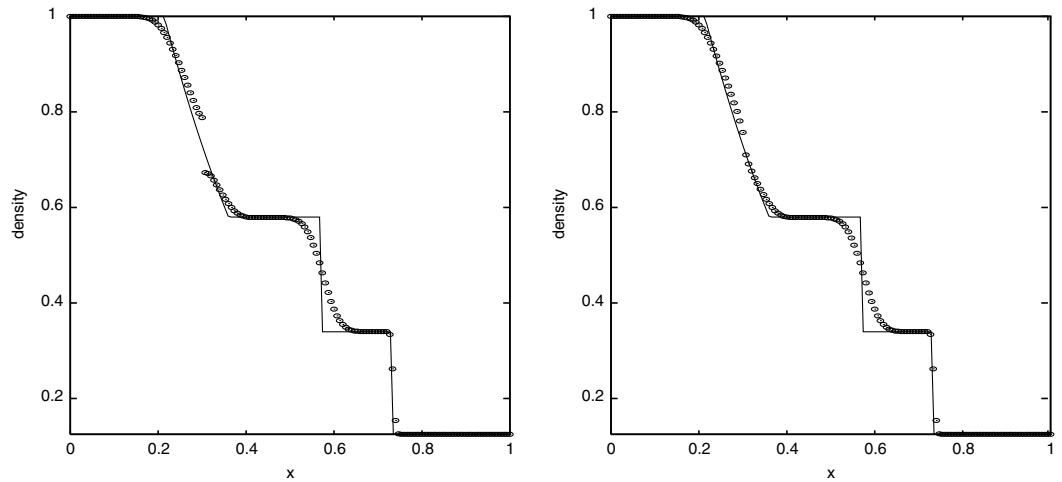

Fig. 21. Same as Fig. 17, except for the Roe scheme with an entropy fix. Left: $\epsilon = 0$; right: $\epsilon = 0.1$.

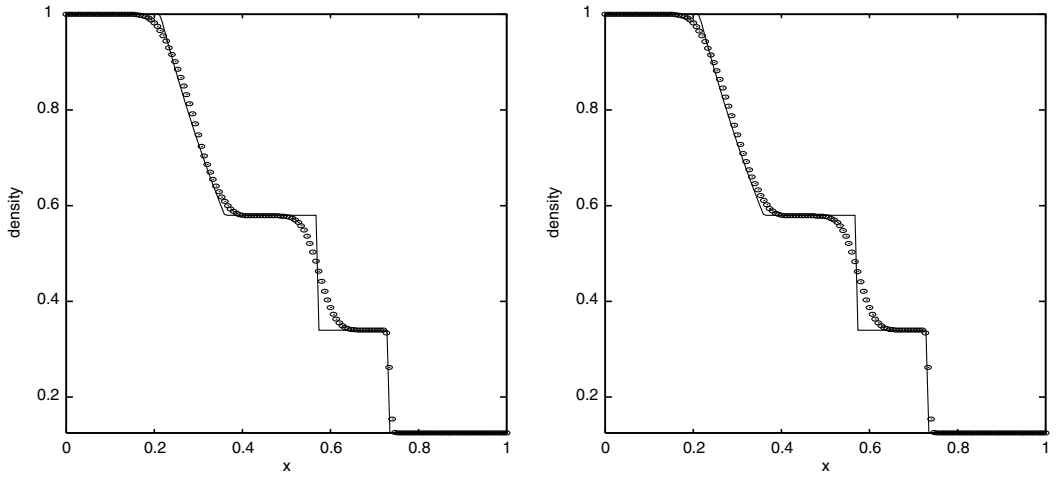

Fig. 22. Same as Fig. 21, except with different ϵ. Left: $\epsilon = 0.2$; right: $\epsilon = 0.3$.

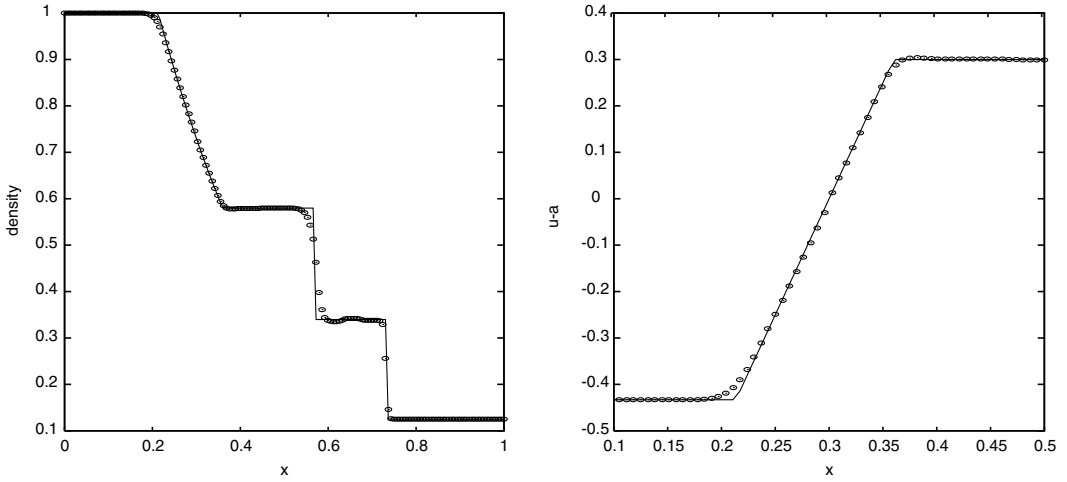

Fig. 23. Same as Fig. 17, except for the MUSCL scheme with Roe approximate solver. Left: the density distribution; right: the characteristic wave speed $u - a$ in the rarefaction wave.

In order to avoid the sonic glitch, there still are several different ways to work with.

(a) Change the numerical wave speed. For example, a numerical sound speed $\widetilde{a} = \sqrt{3p/\rho}$ is introduced in the Beam scheme [19] and the left moving particle has a velocity $u - \sqrt{3p/\rho}$, which does not go to zero in the rarefaction wave, see the left pictures in Figs. 25 and 26, which are showing the density calculated by the Beam scheme and corresponding error.

(b) Do not use the discrete wave speeds $u - a$, u and $u + a$ in the flux construction at all. For example, the LxF scheme and the gas-kinetic scheme including the BGK scheme [30] and the KFVS or EFM scheme [16,12]. The LxF scheme is a central-differencing method, while the gas-kinetic scheme uses a continuous gas distribution equation in the flux evaluation and thus are not fully upwind-differencing in the sense that there is always a relatively small contribution from downstream even if the local Mach number is greater than 1 [11]. Based on kinetic terms, Moschetta and Gressier proposed a cure for the sonic

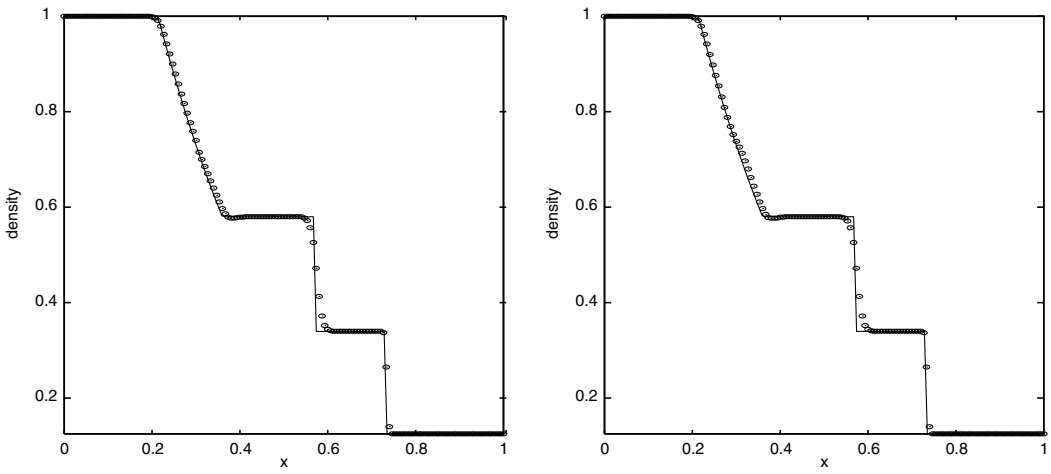

Fig. 24. The density distributions of the Toro's shock tube problem calculated by using the Harten UNO scheme combining the Roe approximate solver with an entropy fix. Left: $\epsilon = 0$; right: $\epsilon = 0.2$.

point glitch in [10]. Their cure does not add dissipation to the original scheme and has been validated in two-dimensional case. The right pictures in Figs. 25 and 26 show the density obtained by using the kinetic FVS scheme and corresponding error.

(c) Use the Eulerian–Lagrangian method, where the characteristic wave speed is changed in a local reference of frame following the fluid motion, and will never become zero. Consequently, the sonic point glitch can never occur in Lagrangian computation, as demonstrated by Hui and Kudriakov [7]. They have computed the Toro's shock tube problem using the Godunov method in Lagrangian coordinate.

In the two-dimensional simulation, due to the implementation of one-dimensional Riemann solver in both directions, across the sonic line the disparity in the wave speed generates the "dog-leg" phenomenon. The non-smoothness of the flow distribution at the sonic point is basically from the upwind flux evaluation method in the shock capturing schemes. At the sonic point, there is no any intrinsic difference between the

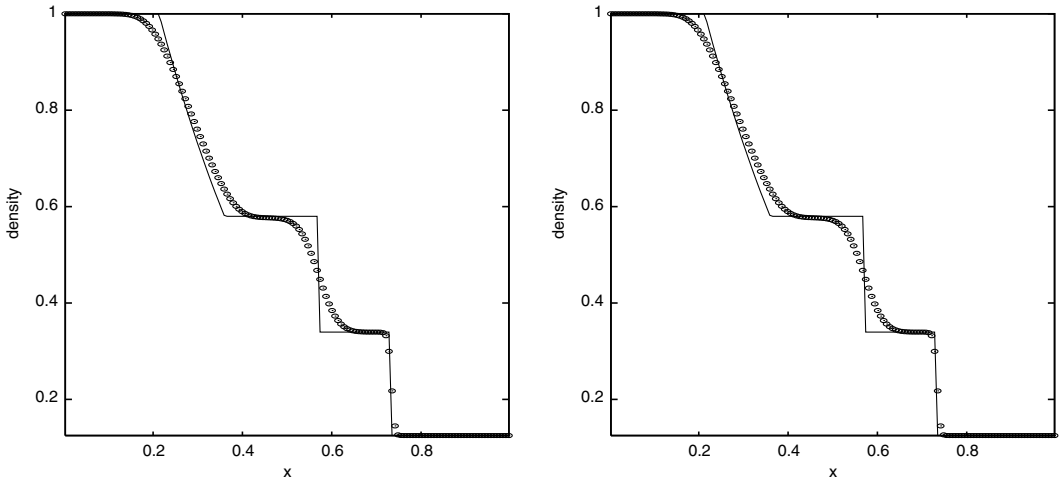

Fig. 25. Same as Fig. 18, except for the Beam method (left) and the kinetic FVS scheme (right).

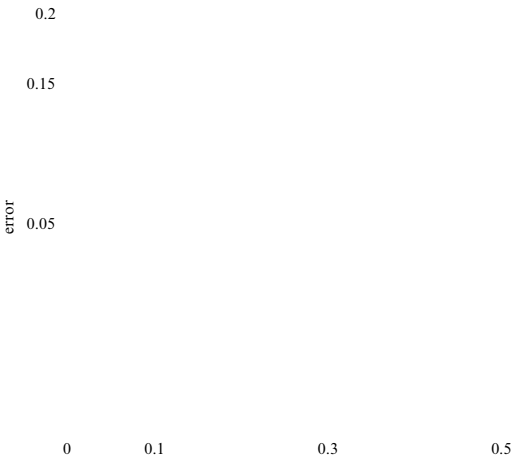

Fig. 26. Close-up of the error, $(\lambda_1)_{j+\frac{1}{2}} - (\lambda_1)^{e}_{j+\frac{1}{2}}$, for the Beam method (left) and the kinetic FVS scheme (right).

Godunov method and many other upwind schemes, such as the Steger–Warming FVS scheme, the van Leer FVS scheme, the Roe approximate Riemann solver, and the Engquist–Osher scheme, because they all depend closely on the characteristic direction. We have used several schemes to solve the problem of a Mach 3 wind tunnel with a forward step, see [29] for a detailed description of this problem. Figs. 27–29 show the density contours with 32 equally spaced contour lines calculated by using the first-order accurate S–W FVS scheme, the second-order accurate MUSCL type Godunov scheme, and the second-order accurate MUSCL type S–W FVS scheme on a uniform grid with $\Delta x = \Delta y = 1/200$, respectively. The ''dog-leg'' phenomenon is efficiently decreased by using the MUSCL technique, although numerical oscillation has been generated by using the MUSCL type Godunov scheme. The sonic glitch is obviously observed in Fig. 27 near the sonic line just above the corner of the forward step.

4. Concluding remarks

In this paper, we have analyzed theoretically and numerically several numerical schemes for the Burgers' equation and the Euler equations in order to give an explanation for the sonic point glitch.

Our results show that there is no any direct connection between the sonic glitch and the violation of the entropy condition of a numerical scheme. Even for an entropy-satisfying scheme, such as the Godunov method, the Engquist–Osher scheme, and the weighted average schemes, the sonic glitch is still formed. With an entropy fix, we may smear out the jump around the sonic point, but in theory, we cannot completely eliminate the error within the sonic rarefaction waves, except with a relatively large parameter.

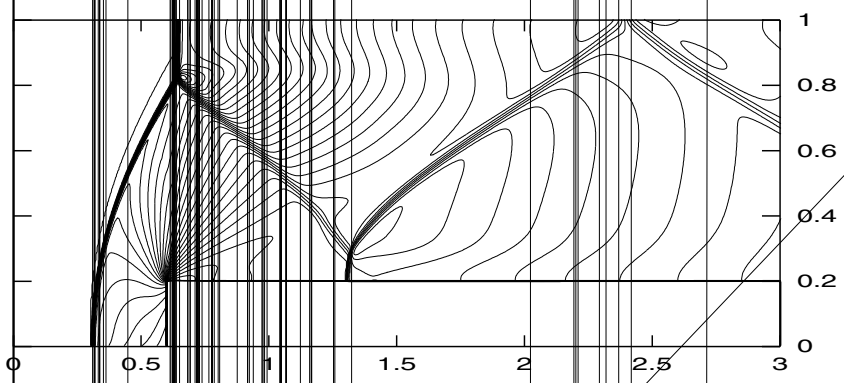

Fig. 27. Same as Fig. 1, except for the S–W FVS scheme.

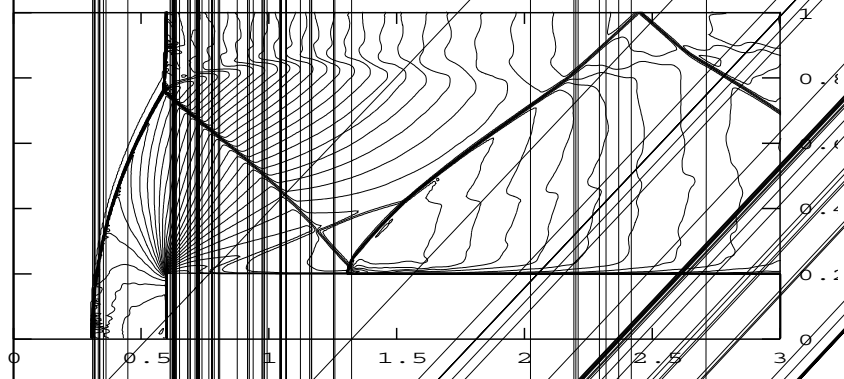

Fig. 28. Same as Fig. 1, except for the MUSCL type Godunov scheme.

transonic expansion fan. But, the high resolution schemes of Harten cannot eliminate completely the error in the sonic rarefaction wave, although they can decrease it. It is still difficult to extend this result to the Euler equations.

Several other possible cures have also been considered, for example: (1) to use the "exact" wave speed to replace the approximate one; (2) to change the numerical wave speed such as the Beam scheme; (3) not to use the discrete characteristic wave speeds $u - a$, u and $u + a$ in the flux construction at all, such as the LxF scheme and the gas-kinetic scheme; and (4) to use the Eulerian–Lagrangian method, where the characteristics wave speed is changed in a local reference of frame following the fluid motion.

Acknowledgments

The author thanks K. Xu for his interesting discussion and preparing our old manuscript [23], and W.W. Liou, J.M. Moschetta, and B. van Leer for their sending him their related papers. The author also want to thank unknown referees for suggesting more numerical examples as well as correcting English errors in the manuscript. This research was partially supported by the Special Funds for Major State Basic Research Projects of China (G1999032801), Key Program of the National Natural Science Foundation of China, and the Alexander von Humboldt foundation.

References

[1] J.D. Anderson, Modern Compressible Flow with Historical Perspective, McGraw-Hill, New York, 1990.
[2] S.F. Davis, A simplified TVD finite difference scheme via artificial viscosity, SIAM J. Sci. Stat. Comput. 8 (1987) 1–18.
[3] B. Engquist, S. Osher, One sided difference approximations for nonlinear conservation laws, Math. Comp. 36 (1981) 321–351.
[4] S.K. Godunov, A finite difference method for the computation of discontinuous solutions of the equations of fluid dynamics, Mat. Sb. 47 (1959) 271–306.
[5] A. Harten, High resolution schemes for hyperbolic conservation laws, J. Comput. Phys. 49 (1983) 357–393.
[6] C. Hirsch, Numerical Computation of Internal and External Flows, vols. 1 and 2, Wiley, New York, 1990.
[7] W.H. Hui, S. Kudriakov, On wall overheating and other computational difficulties of shock-capturing methods, CFD J. 10 (2001) 192–209.
[8] M.S. Liou, C.J. Steffen, A new flux splitting scheme, J. Comput. Phys. 107 (1993) 23–39.
[9] F.J. Liu, W.W. Liou, A new approach for eliminating numerical oscillations of Roe family of schemes at sonic point, AIAA 99-0301, in: 37th AIAA Aerospace Sciences Meeting and Exhibit, Reno, NV, 1999.
[10] J.M. Moschetta, J. Gressier, The sonic point glitch problems: a numerical solution, in: Charles-Henri Bruneau (Ed.), 16th International Conference on Numerical Methods in Fluid Dynamics, 1998, pp. 403–408.
[11] J.M. Moschetta, J. Gressier, A cure for the sonic point glitch, Int. J. Comput. Fluid Dynamics 13 (2000) 143–159.
[12] J.-M. Moschetta, D.I. Pullin, A robust diffusive kinetic scheme for the Navier–Stokes/Euler equations, J. Comput. Phys. 133 (1997) 193–204.
[13] J.J. Quirk, A contribution to the great Riemann solver debate, Int. J. Numer. Methods Fluids 18 (1994) 555–574.
[14] S. Osher, F. Solomon, Upwind difference schemes for hyperbolic conservation laws, Math. Comp. 38 (1982) 339–374.
[15] S. Osher, S. Chakravarthy, Upwind schemes and boundary conditions with applications to Euler equations in general geometries, J. Comput. Phys. 50 (1983) 447–481.
[16] D.I. Pullin, Direct simulation methods for compressible inviscid ideal gas flow, J. Comput. Phys. 34 (1980) 231–244.
[17] P.L. Roe, Approximate Riemann solvers, parameter vectors, and difference schemes, J. Comput. Phys. 43 (1981) 357–372.
[18] P.L. Roe, Sonic flux formulae, SIAM J. Sci. Stat. Comput. 13 (1992) 611–630.
[19] R. Sanders, K. Prendergast, The possible relation of the three-kiloparsec arm to explosions in the galactic nucleus, Astrophys. J. 188 (1974) 489–500.
[20] J.L. Steger, R.F. Warming, Flux vector-splitting of the inviscid gas dynamic equations with applications to finite difference methods, J. Comput. Phys. 40 (1981) 263–293.
[21] H.Z. Tang, T. Tang, Adaptive mesh methods for one- and two-dimensional hyperbolic conservation laws, SIAM J. Numer. Anal. 41 (2003) 487–515.

[22] H.Z. Tang, K. Xu, Pseudoparticle representation and positivity analysis of explicit and implicit Steger–Warming FVS schemes, Z. Angew. Math. Phys. 52 (2001) 847–858.
[23] H.Z. Tang, K. Xu, An explanation for the sonic point glitch, preprint, 2000. Available from: <http://www.math.ntnu.no/conservation/>.
[24] E.F. Toro, Riemann Solvers and Numerical Methods for Fluid Dynamics, second ed., Springer, Berlin, 1999.
[25] B. van Leer, Towards the ultimate conservative difference scheme V. A second order sequel to Godunov's method, J. Comput. Phys. 32 (1979) 101–136.
[26] B. van Leer, Flux-vector splitting for the Euler equations, Technical Report ICASE 82-30, NASA Langley Research Center, USA, 1982. Also in Proceedings of the 8th International Conference on Numerical Methods in Fluid Dynamics, Springer, Berlin, 1982, pp. 507–512.
[27] B. van Leer, On the relation between the upwind-differencing schemes of Godunov, Engquist–Osher and Roe, SIAM J. Sci. Stat. Comput. 5 (1984) 1–20.
[28] B. van Leer, W.T. Lee, K.G. Powell, Sonic-point capturing, AIAA-89-1945-CP, in: AIAA 9th Computational Fluid Dynamics Conference, Buffalo, NY, 1989.
[29] P. Woodward, P. Colella, The numerical simulation of two-dimensional fluid flow with strong shocks, J. Comput. Phys. 54 (1984) 115–173.
[30] K. Xu, Gas-Kinetic Schemes for Unsteady Compressible Flow Simulations, VKI Fluid Dynamics Lecture Series, 1998-03, 1998. Available from: <http://www.math.ust.hk/~makxu>.